DHCR24-mediated sterol homeostasis during spermatogenesis is required for sperm mitochondrial sheath formation and impacts male fertility over time

Sona Relovska[1†], Huafeng Wang[1†], Xinbo Zhang[2,3], Pablo Fernández-Tussy[2,3], Kyung Jo Jeong[4], Jungmin Choi[4,5], Yajaira Suárez[2,3,6], Jeffrey G. McDonald[7,8], Carlos Fernández-Hernando[2,3,6*], Jean-Ju Chung[1,9*]

[1]Department of Cellular and Molecular Physiology, Yale School of Medicine, New Haven, CT 06510, USA; [2]Department of Comparative Medicine, Yale University School of Medicine, New Haven, CT 06510, USA; [3]Vascular Biology and Therapeutics Program, Yale University School of Medicine, New Haven, CT 06510, USA; [4]Department of Biomedical Sciences, Korea University College of Medicine, Seoul, South Korea; [5]Department of Genetics, Yale School of Medicine, Yale University, New Haven, Connecticut, USA; [6]Department of Pathology, Yale University School of Medicine, New Haven, CT 06510, USA; [7]Department of Immunobiology, Yale University School of Medicine, New Haven, CT 06510, USA; [8]Center for Human Nutrition, University of Texas Southwestern Medical Center, Dallas, TX 75390; [9]Department of Gynecology and Obstetrics, Yale School of Medicine, New Haven, CT 06510, USA

[†]Equal contribution

[*]For correspondence: carlos.fernandez@yale.edu; jean-ju.chung@yale.edu

Keywords: spermatozoa, 24-dehydrocholesterol reductase, male infertility, cholesterol, sterol homeostasis, mitochondrial packing, cellular metabolism

Abstract

Desmosterol and cholesterol are essential lipid components of the sperm plasma membrane. Cholesterol efflux is required for capacitation, a process through which sperm acquire fertilizing ability. In this study, using a transgenic mouse model overexpressing 24-dehydrocholesterol reductase (DHCR24), an enzyme in the sterol biosynthesis pathway responsible for the conversion of desmosterol to cholesterol, we show that disruption of sterol homeostasis during spermatogenesis led to defective sperm morphology characterized by incomplete mitochondrial packing in the midpiece, reduced sperm count and motility, and a decline in male fertility with increasing paternal age, without changes in body fat composition. Sperm depleted of desmosterol exhibit inefficiency in the acrosome reaction, metabolic dysfunction, and an inability to fertilize the egg. These findings provide molecular insights into sterol homeostasis for sperm capacitation and its impact on male fertility.

Introduction

Lipids are essential for mammalian fertility, contributing to both steroidogenesis (Miller et al., 2011) and germ cell formation (Shi et al., 2018). In humans and other mammalian species, cholesterol and desmosterol are major sterol components of the sperm plasma membrane (Keber et al., 2013). To gain fertilization capability, the sperm plasma membrane undergoes changes that result in cholesterol efflux, allowing sperm to undergo capacitation, including the acrosome reaction (Leahy and Gadella, 2015). An appropriate species-dependent sterol composition of the sperm plasma membrane is essential for successful fertilization. Coincidentally, male obesity has been linked to reduced reproductive success and infertility in both humans (Leisegang et al., 2020, Craig et al., 2017) and animal models (Ghanayem et al., 2010; Borges et al., 2017; Han et al., 2023). During spermiation, when mature spermatids dissociate from Sertoli cells and enter the lumen of the seminiferous tubules, the cholesterol content of the sperm plasma membrane decreases. This reduction continues as sperm migrate through the epididymis and acquire fertilizing capacity (Nikolopoulou et al., 1985; Haidl and Opper, 1997). During sperm capacitation, the plasma membrane becomes more fluid, and cholesterol relocates to the apical margin of the sperm head before eventually translocated to the extracellular environment by albumin (Leahy and Gadella, 2015). A study in boar and mouse sperm demonstrated the importance of sterol oxidation and oxysterol formation, which is dependent on the bicarbonate-induced reactive oxygen species (ROS) signaling pathway, for sterol removal from the plasma membrane during capacitation (Boerke et al., 2013). In sperm samples from infertile men, elevated levels of both cholesterol and its immediate precursor desmosterol were observed, but the cholesterol/desmosterol ratio was decreased (Zalata et al., 2010), suggesting that sperm sterol homeostasis is essential for male fertility in humans. However, the specific impact of the disruption of sterol homeostasis on sperm physiology remains largely unknown.

Two parallel pathways contribute to cellular cholesterol biosynthesis from lanosterol. Both pathways – the Bloch pathway and the Kandutsch-Russell pathways – are interconnected by the enzyme DHCR24, which reduces the double bond in the side chain of all Bloch pathway sterols and converts them to the Kandutsch-Russel pathway sterols (Figure 1A). Notably, DHCR24 activity in various tissues is essential for the production of diverse bioactive sterols, crucial for maintaining cellular homeostasis and tissue physiology. The *Dhcr24*-null mouse model exhibits nearly undetectable levels of plasma cholesterol and abnormally high levels of desmosterol, leading to increased prenatal mortality, poor growth in males that persists into adulthood, degenerated testes, and infertility in both males and females (Wechsler et al., 2003). In humans, mutations in the *DHCR24* gene cause desmosterolosis, a rare congenital disorder characterized by excessive desmosterol and insufficient cholesterol. This condition also affects brain and head development and causes cardiac malformations and arthrogryposis (FitzPatrick et al., 1998; Andersson et al., 2002; Schaaf et al., 2011; Zolotushko et al., 2011; Dias et al., 2014; Rohanizadegan & Sacharow, 2018; Hill et al., 2023). Our previous studies demonstrated that DHCR24 overexpression in myeloid cells depletes desmosterol, increases inflammation and mitochondrial ROS production, and impairs LXR/RXR pathway activation (Zhang et al., 2021[a]).

In this study, we report that whole-body overexpression of DHCR24 (*Dhcr24-TG*) leads to decreased fertility with reduced sperm count and motility in male mice, correlated with increasing paternal age. DHCR24 overexpression depletes sperm desmosterol and disrupts plasma membrane sterol homeostasis. Scanning and transmission electron microscopy of *Dhcr24-TG* spermatozoa revealed defects in the mitochondria and sperm tail, including incomplete mitochondrial packing and bent tails. IZUMO staining showed reduced efficiency of *Dhcr24-TG* sperm to undergo the acrosome reaction during capacitation, even in spermatozoa from young adult males. Furthermore, our findings suggest that

91 metabolically, uncapacitated *Dhcr24-TG* sperm resemble capacitated sperm in their increased oxygen
92 consumption and faster depolarization of mitochondrial membrane potential. Taken together, our results
93 demonstrate that desmosterol depletion and/or altered sterol homeostasis during spermatogenesis
94 impacts sperm morphology, number, motility, and metabolism, leading to reduced male fertility.

Results

DHCR24 overexpression leads to an age-dependent decline in male fertility

In our previous study, we generated a myeloid-specific conditional knock-in mouse line overexpressing DHCR24 (Figure 1A) (Zhang et al., 2021). Here, we used a similar approach to generate a global *Dhcr24* transgenic mouse line by breeding the *Dhcr24*$^{fl/fl}$ mice (overexpression of the construct in the *Rosa26* genetic locus) with the *EIIa*^{CRE} mice (which express *Cre recombinase* in the early mouse embryo) (Figure 1–figure Supplement 1A). We used male mice aged 2 to 10 months, categorizing them as young (2-4 months old), mature (5-7 months old) and middle-aged (8-10 months old) adults (adapted from Flurkey et al., 2007). After establishing mating between wild-type (WT) and *Dhcr24-TG* (TG) animals, using young and mature adult males and young adult females, we found that mature adult TG males sired significantly smaller litters than young adult TG males, with no alterations in the pup sex ratio (Figure 1B, Figure 1–figure supplement 1B). Moreover, they exhibited delay in impregnating the females (Figure 1–figure supplement 1C). In contrast, WT males displayed no fertility changes within this age range. In light of these observations, we delved into exploring the consequences of desmosterol depletion through DHCR24 overexpression on sperm physiology.

Analyzing publicly available human (GSE109037) and mouse (GSE109033) testis scRNA-seq data, we found that *DHCR24* mRNA in human testis is most abundantly expressed in spermatogonia and, to a lesser extent, in spermatocytes and late spermatids (Figure 1C). This pattern mirrors *Dhcr24* mRNA levels in mouse adult and postnatal day 6 (P6) testis (Figure 1D), where it is most abundant in spermatogonia and to a lesser extent in Sertoli cells and peritubular myoid cells. We examined DHCR24 protein expression in WT and TG testes and found increased protein level in samples from TG animals (Figure 1–figure supplement 1D). In line with the scRNA-seq data, DHCR24 is not readily detected in WT spermatozoa, but is detected in young adult TG spermatozoa from caput, corpus and cauda epididymis, and to a lesser extent in mature adult TG spermatozoa (Figure 1E). Collectively, these data demonstrate DHCR24 expression in male germ cells and suggest that disruption of sterol synthesis during spermatogenesis may explain the observed decline of male fertility in *Dhcr24-TG* animals.

DHCR24 overexpression leads to dysregulation of sperm sterol composition and capacitation efficiency

Alterations in sperm cholesterol, desmosterol, and the cholesterol to desmosterol ratio have been associated with subfertility in men (Zalata et al., 2010). To assess changes in sperm sterol composition, we measured specific sterols in the Bloch and Kandutsch-Russel pathways in spermatozoa from mature adult WT and TG males. In the Bloch pathway, we observed decreased levels of desmosterol (Des), 7-dehydrodesmosterol (7-DHD), and zymosterol (ZyE) (Figure 2A). In the Kandutsch-Russell pathway, both immediate cholesterol precursors –7-dehydrocholesterol (7-DHC) and 8,9-dehydrocholesterol (8-DHC)– showed decreased levels compared to WT sperm. Notably, the levels of 24,25-dihydrolanosterol (24,25DHLan) were significantly increased albeit just above the detection range (Figure 2B). Although we did not directly measure sperm cholesterol by the mass spectrometry, we speculated that cholesterol might be increased in TG sperm, considering the predominant flux (97%) through the Bloch pathway in the testis (Mitsche et al, 2015, eLife). However, our results indicated no statistical difference in cholesterol levels isolated from the whole testis of young adult and mature adult WT or Dhcr24-TG males (Figure 2C). This is consistent with our findings of no significant changes in mRNA expression in *Abca1* cholesterol transporter in the testis of young adult and mature adult WT and *Dhcr24-TG* males, nor *Nr1h2* and *Nr1h3,* which encode the ABCA1 transcriptional regulators, LXRβ and LXRα, respectively, (Figure 2–figure

138 supplement 2A). Additionally, the ABCA1 protein levels remained unchanged (Figure 2–figure supplement
139 2B). Furthermore, EchoMRI results showed no changes in the fat mass to lean mass ratio in middle-aged
140 TG males (Figure 2–figure supplement 3A), consistent with unchanged plasma cholesterol levels between
141 young adult WT and *Dhcr24-TG* males (Figure 2–figure supplement 3B), further supporting these findings.
142 To determine whether the altered sterol composition of TG sperm affects their ability to undergo
143 the acrosome reaction, we incubated them in the absence or presence of bovine serum albumin (BSA) or
144 methyl-β-cyclodextrin (MBCD), both acting as a cholesterol sink during capacitation, with MBCD even
145 more efficiently than BSA (Visconti et al., 1999). As cholesterol efflux is required for the acrosome reaction
146 to occur in a timely manner (Leahy and Gadella, 2015), fixed spermatozoa were immunostained for IZUMO
147 to examine the status of acrosome reaction. We found that TG spermatozoa did not undergo acrosome
148 reaction as efficiently as WT spermatozoa, *i.e.,* the proportion of partially reacted TG spermatozoa was
149 higher (Figure 2D). These observations align with the experiment using spermatozoa from middle-aged
150 adult animals, where a greater proportion of TG spermatozoa were only partially acrosome-reacted than
151 WT spermatozoa (Figure 2–figure supplement 3C). Notably, even sperm from young adult TG males
152 demonstrated reduced efficiency during *in vitro* fertilization (IVF). When TG sperm were capacitated at a
153 high concentration ($20x10^6$ cells/mL), the 2-cell cleavage rate dropped below 10%, whereas WT sperm still
154 fertilized the oocytes with over 80% cleavage rate (Figure 2E). In contrast, TG sperm capacitated at the
155 standard concentration used for IVF ($2x10^6$ cells/mL) fertilized the oocytes at 80%. Taken together, these
156 results demonstrate that altered sterol composition affects the efficiency of sperm capacitation and
157 impairs fertility.

158 ***Dhcr24-TG* males have decreased sperm count and motility**

159 As DHCR24 is globally overexpressed in our TG animals and not specifically in male germ cells, we
160 investigated whether the changes in sterol composition have an impact on spermatogenesis and/or sperm
161 motility. We found a lower epididymal sperm count in young adult TG males, although not statistically
162 significant, but this difference became statistically significant with aging (Figure 3A). Consistently,
163 hematoxylin and eosin staining revealed an overall normal testis histology, but mature adult TG testis and
164 epididymis showed a decrease in sperm count (Figure 3B). To assess sperm total and hyperactivated
165 motility, we utilized the Computer Assisted Sperm Analyzer (CASA) on WT and TG spermatozoa. Both
166 before and after capacitation, spermatozoa from either young or mature adult TG animals displayed
167 reduced motility. Additionally, the hyperactivated motility of TG spermatozoa was also diminished (Figure
168 3C). Similar results were observed in middle-aged adult spermatozoa capacitated in the presence of BSA
169 or MBCD (Figure 3–figure supplement 4A and 4B). Notably, the percentage of hyperactivated WT
170 spermatozoa decreased when capacitated at high concentration (5.1%, compared to 16% percent when
171 capacitated at the standard concentration), and the percentage of hyperactivated TG sperm was 3-5 times
172 lower than that of WT, regardless of sperm concentration (1.7% and 2.9% at high and standard
173 concentrations, respectively) (Figure 3–figure supplement 4D). Importantly, sperm concentration during
174 capacitation did not affect the total motility of either WT or TG spermatozoa (Figure 3–figure supplement
175 4C). Flagellar waveform analysis revealed that a fraction of TG spermatozoa exhibited altered flagellar
176 beating that became more prominent during sperm capacitation, presumably due to defective flagellar
177 bending that flips the head backward (Figure 3D, Figure 3–supplementary video 1). These motility defects
178 prompted us to further investigate sperm morphology in more detail.

Desmosterol depletion results in sperm tail bending and aberrant mitochondrial packing

Upon closer examination of our movies, we found that bent TG spermatozoa often exhibited a head curled toward the midpiece and a thinning in the distal midpiece just before the annulus (Figure 3E, Figure 3–supplementary video 1). Co-immunostaining for the outer dense fiber (ODF) component ODF2 and the mitochondrial protein Tom20 indicated defective mitochondrial packing and ODF exposure (Figure 4A). Further examination of TG sperm ultrastructure using scanning electron microscopy (SEM) and transmission electron microscopy (TEM) (Figure 4B and 4D) revealed the inverted heads and thinning of the distal midpiece of TG spermatozoa, which lacked the mitochondrial sheath and exposed the outer dense fiber due to mitochondrial sheath shortening (Figure 4B and 4C). Quantification and classification of mitochondrial unraveling and tail bending defects from the SEM images confirmed the increased instances of aberrant mitochondrial packing and defective structural integrity of TG spermatozoa (Figure 4D). TEM images further supported these findings, revealing defective mitochondrial structure and packing along the sperm tails in TG spermatozoa (Figure 4D).

Defective mitochondria in *Dhcr24-TG* males cause alteration in sperm metabolism

Having observed defects in mitochondrial structure in TG sperm, we next set out to investigate mitochondrial function. Spermatozoa must meet high energy demands as they travel to deliver the paternal genome to the oocyte. ATP production in spermatozoa occurs through two spatially compartmentalized metabolic processes in the tail: mitochondrial oxidative phosphorylation (OXPHOS) in the midpiece and glycolysis from the principal piece (Visconti, 2012). We measured sperm mitochondrial membrane potential (ΔΨm) using MitoTracker Red CMXRos dye (Pendergrass et al., 2004; Santiani et al., 2016), followed by antimycin treatment (Figure 5A), as previously described (Ferreira et al., 2021; Wang et al., 2022). We found that uncapacitated TG sperm from young adult males exhibited similar ΔΨm depolarization to capacitated WT and TG sperm after antimycin treatment – faster and to a greater extent than that of uncapacitated WT sperm (Figure 5B). This suggests a metabolic similarity of uncapacitated TG sperm to capacitated sperm. There was no difference in the rate or amplitude of membrane depolarization of the capacitated spermatozoa. To investigate whether this change affects oxygen consumption rate (OCR), we measured extracellular flux using Seahorse. Basal respiratory OCR, the difference between the initial and post-antimycin/rotenone injection measurements, increased after incubation under capacitating conditions, consistent with previous reports (Balbach et al., 2020, Ferreira et al., 2021). Interestingly, TG sperm from middle-aged males exhibited higher basal respiratory OCR in both uncapacitated and capacitated conditions (Figure 5C; Figure 5–figure supplement 5), suggesting that uncapacitated TG spermatozoa have higher metabolic demands and are more comparable to capacitated spermatozoa, in line with our observations from ΔΨm measurements.

In summary, desmosterol depletion and the consequent sterol imbalance results in an age-dependent decline in male fertility, partly due to reduced sperm count and motility with mitochondrial structural and functional defects.

Discussion

Dysregulation of lipid metabolism affects male fertility

Wechsler *et al.*, (2003) previously reported that loss of DHCR24 function results in infertility in both female and male mice, with testicular abnormalities observed in *Dhcr24*$^{-/-}$ male mice. In this study, we report that gain of DHCR24 function, leading to desmosterol depletion, renders males subfertile and this condition worsens with age, while females remain fertile. Interestingly, an age-associated decline in male fertility

222 has been reported in several other mouse models with dysregulated cholesterol homeostasis. Examples
223 include ATP-binding cassette transporter 1 (ABCA1), a lipid transporter responsible for the efflux of excess
224 cholesterol and phospholipids from Sertoli cells in the testis (Selva *et al.*, 2004; Morales *et al.*, 2008), and
225 liver X receptor/retinoid X receptor (LXR/RXR) (Volle *et al.*, 2007), which regulates ABCA1 expression
226 (Venkateswaran *et al.*, 2000; Costet *et al.*, 2000). Consistently, lipid droplets accumulated in Sertoli cells of
227 *Abca1*$^{-/-}$ males, reducing their fertility by 6 months of age with decreased sperm count and testosterone
228 levels (Selva *et al.*, 2004). Similarly, accumulation of cholesterol/lipid droplets was observed in the testes
229 of LXR-β-null males with age-dependent spermatogenesis defects (Robertson *et al.,* 2005). Since our
230 previous study showed that desmosterol depletion in macrophages resulted in impaired LXR activation
231 and lipid accumulation as well as reduced ABCA1 levels (Zhang et al., 2021a), we initially speculated that
232 impaired LXR/RXR activation and/or ABCA1 expression might contribute to the phenotypes we observed
233 in *Dhcr24-TG* males. However, our data comparing *Nr1h2* (LXRβ), *Nrhh3* (LXRα), and *Abca1* mRNA levels,
234 as well as ABCA1 protein levels in the testes of WT versus TG animals showed no significant changes in
235 either young or mature adult males (Figure 2–figure supplement 2A and 2B). It is possible that desmosterol
236 does not transcriptionally activates LXR in the mouse male reproductive system, or that desmosterol-
237 regulated LXR signaling only manifests in animals fed a high fat diet and/or overweight animals, but these
238 factors may not be responsible for the observed phenotype in our *Dhcr24-TG* mouse model. Similarly,
239 desmosterol does not activate LXR in hepatocytes (Muse *et al.*, 2018), suggesting that this intermediate of
240 cholesterol biosynthesis is a specific LXR ligand in myeloid cells, but not in other cells and tissues (Muse *et*
241 *al.*, 2018; Spann *et al.*, 2012; Zhang *et al.*, 2021a).
242 Notably, DHCR24 overexpression in our mouse model had no observable effect on body fat mass
243 (Figure 2–figure supplement 3A) or plasma cholesterol levels (Figure 2–figure supplement 3B).
244 Consistently, there were only marginal changes in the immediate cholesterol precursors 7-DHC and 8,9-
245 DHC in spermatozoa (Figure 2B), and no differences in the cholesterol levels isolated from the testis (Figure
246 2C). These findings are likely attributed to the negative feedback mechanisms that occur during
247 spermatogenesis and spermiogenesis, ensuring the maintenance of appropriate cholesterol levels, given
248 its crucial role. Furthermore, the normal fat to lean mass ratio in *Dhcr24-TG* mice rules out any known
249 effects of obesity on male fertility, such as increased inflammation or abnormalities in hormone synthesis
250 (Katib, 2015, Han et al., 2023). Instead, the observed defects result directly from an imbalance in cellular
251 cholesterol homeostasis, specifically desmosterol depletion. A previous study indicated alterations in the
252 desmosterol to cholesterol ratio in sperm from infertile men (Zalata et al., 2010). Thus, the sterol
253 imbalance in the *Dhcr24-TG* spermatozoa itself is likely the cause of the delayed acrosome reaction.
254 Additionally, the global defects in lipid signaling, levels of desmosterol, and other cholesterol precursors
255 in the testis and plasma may affect spermatogenesis or spermiogenesis, contributing to the observed
256 sperm defects and reduced sperm counts in *Dhcr24-TG* animals.

257 **Desmosterol-depleted sperm show defective cellular metabolism**

258 We found abnormalities in the tail structure of sperm from *Dhcr24-TG* animals, particularly in the
259 midpiece, as evidenced by mitochondrial packing defects and abnormally bent tail (Figure 4). It remains
260 unclear whether these defects result from issues during spermatogenesis/spermiogenesis or are caused
261 by changes in the lipid composition of the sperm plasma membrane and/or the mitochondrial membrane.
262 Notably, these mitochondrial structural changes are associated with alterations in cellular metabolism in
263 uncapacitated *Dhcr24-TG* spermatozoa. In previous studies, elevated OXPHOS levels are found in diabetic
264 cardiac microvascular endothelial cells (CMECs), correlated with increased intracellular ROS (Zhang et al.,
265 2021b). We previously showed that desmosterol depletion in macrophages also leads to ROS accumulation

266 (Zhang et al., 2021a). In spermatozoa, mitochondria are a source of ROS with a dual function: ROS is a
267 signaling molecule during capacitation (O'Flaherty et al., 2006, Boerke et al., 2013), but high levels of ROS
268 have the potential to damage sperm DNA and negatively affect fertility (Aitken and Baker, 2006). Complex
269 I and complex III are recognized as the major ROS producers in spermatozoa (Koppers et al., 2008). Our
270 OXPHOS measurements revealed an increase in basal OCR levels in uncapacitated *Dhcr24-TG*
271 spermatozoa, approaching levels similar to capacitated WT spermatozoa (Figure 5C). Furthermore,
272 uncapacitated *Dhcr24-TG* sperm membranes are depolarized after antimycin treatment at rates similar to
273 those observed in capacitated WT and *Dhcr24-TG* spermatozoa (Figure 5B). The sensitivity to antimycin in
274 uncapacitated *Dhcr24-TG* spermatozoa and increased MMP could be explained by increased complex III
275 activity, potentially leading to increased ROS production, which in turn may contribute to the observed
276 sperm defects in TG spermatozoa.
277
278 In this study, we utilized a mouse model with DHCR24 overexpression to induce desmosterol
279 deficiency, aiming to investigate significance of sterol homeostasis in sperm function and fertility, and
280 explore the effects of sterols on sperm cell metabolism. Our findings revealed alterations in the sperm
281 sterol composition, resulting in morphological and metabolic defects of spermatozoa, ultimately leading
282 to impaired fertility. This underscores the impact of sterol imbalance on the fertilization ability of
283 spermatozoa. Interestingly, we observed increased OCR and MMP. Whether *Dhcr24-TG* sperm accumulate
284 more ROS as a result of sterol dysfunction remains to be investigated in the future. Importantly, our results
285 establish a connection between cellular metabolism and sterol homeostasis, specifically highlighting the
286 role of desmosterol. Furthermore, our studies suggest that deviations in sterol homeostasis may not
287 always be correlated with obesity, at least in mice. If this finding extends to humans, it could have
288 implications for how we understand and study sterol dysregulation and its relationship with infertility.
289 Single nucleotide polymorphisms in genes encoding enzymes important for sterol synthesis may impact
290 male fertility, even in the absence of increased body fat, while obesity in these individuals could worsen
291 fertility outcomes.
292

293 ## Materials and Methods

294 ### Generation of *Dhcr24*$^{fl/fl\text{-}CRE}$ (*Dhcr24-TG*) knock-in mice

295 Homozygous *Dhcr24*$^{fl/fl}$ mice were crossed with the transgenic mice expressing Cre recombinase under the
296 control of the EIIa promoter (JAX stock #003724) that targets expression of Cre recombinase to the early
297 mouse embryo to induce germ line deletion of loxP flanked sites. *Dhcr24*$^{fl/fl\text{-}CRE}$ (*Dhcr24-TG*) mice were
298 compared to *Dhcr24*$^{fl/fl}$ used as WT control group.

299 ### Plasma cholesterol concentration measurements

300 Blood samples from young adult males were collected by retroorbital venous plexus puncture or cardiac
301 puncture if terminal, after 6h fasting. Plasma was separated by centrifugation and stored at -80°C until
302 analysis. Total plasma cholesterol levels were determined by standard enzymatic methods (Wako
303 Chemicals).

304 ### Antibodies and reagents

305 All antibodies and reagents used in this study are commercially available and listed in the key resource
306 table. All the chemicals were from Sigma Aldrich unless indicated.

Fertility test

Mating test

Wild type or *Dhcr24-TG* female mice were caged with biallelic *Dhcr24-TG* males for up to 4 months to record pregnancy and litter size when they gave births.

In vitro fertilization assay

The whole procedure was carried out using TYH media (in mM: 119.37 NaCl, 4.78 KCl, 1.19 KH_2PO_4, 5.56 glucose, 1 sodium pyruvate, 1.19 $MgSO_4$, 25.07 $NaHCO_3$, 1.71 $CaCl_2$) supplemented with 0.0005% phenol red and 4 mg/mL of lipid rich BSA AlbuMax (Thermo Fisher). Young adult male mice were euthanized by CO_2 and cervical dislocation. Sperm from one epididymis was released into TYH, and either capacitated for 1-1.5 hours without further dilution (final concentration 14-20x10^6 sperm/mL) or diluted to concentration 2x10^6 sperm/mL for capacitation. 7–10-week-old female B6D2F1 mice were superovulated by peritoneal injection of 10 IU PMSG 64 hours, and 10 IU hCG 16 hours prior to euthanasia by cervical dislocation. Cumulus-oocyte-complexes were isolated from ampullae of oviducts, placed into 50 µL TYH drop for 45 minutes - 1 hr. 10-20 µL of capacitated sperm were added to a TYH drops containing COCs, and left incubating for 6 hours, after which the fertilizing eggs were washed three times, discarding dying eggs, and incubated at 37°C 5% CO_2 overnight. The next day, cleavage rate was scored based on the formation of 2-cell stage embryos.

Single cell RNA-seq analysis

Existing single cell RNA-seq databases were analyzed as previously described (Hwang et al., 2021). The raw count matrices for human (GSE109037) and mouse (GSE109033) testis single cell RNA (scRNA)-seq datasets (Hermann et al., 2018) were downloaded from Gene Expression Omnibus (GEO) database. The downloaded raw count matrices were processed for quality control using the Seurat package (ver.3.2.3) (Stuart et al., 2019) with cells with <200 expressed features or >9000 (GSE109033) or 10 000 (GSE109037) expressed features, and >20% (GSE109037) or 25% (GSE109033) mitochondrial transcript fraction were excluded. The data was normalized by total expression, scaled and log transformed, and 2000 highly variable features was identified, followed by PCA to reduce the number of dimensions representing each cell. Statistically significant 15 PCs were selected based on the JackStraw and Elbow plots and provided as input for constructing a K-nearest-neighbors (KNN) graph based on the Euclidean distance in PCA space. Cells were clustered by the Louvain algorithm with a resolution parameter 0.1. Uniform Manifold Approximation and Projection (UMAP) was used to visualize and explore cluster data. Marker genes that define each cluster were identified by comparing each cluster to all other clusters using the MAST (Finak et al., 2015) provided in Seurat package. In order to correct batch effects among samples and experiments, the Harmony package was applied (ver.1.0) (Korsunsky et al., 2019) to the datasets. The Markov Affinitybased Graph Imputation of Cells (MAGIC) algorithm (ver.2.0.3) (van Dijk et al., 2018) was used to denoise and the count matrix and impute the missing data. In testis datasets from adult human, we identified 23 896 high quality single cells that were clustered into seven major cell types, namely spermatogonia, spermatocytes, early spermatids, late spermatids, peritubular myoid cell, endothelial cell, and macrophage. Similarly, we identified 30 268 high quality single cells from eight adult and three postnatal day 6 mouse testis tissue samples and subsequently defined 11 major cell populations.

346 **qRT-PCR**

347 RNA was extracted from the testis using RNeasy Mini Kit (Qiagen) according to manufacturer's instructions.
348 Briefly, 20-30 mg of testis in 600 µL of RLT buffer was homogenized using 20G needle attached to a syringe.
349 Samples were transferred into a microtube, centrifuged for 3 minutes 21000 g and supernatant was mixed
350 with 600 µL of 70% ethanol. Mixture was transferred into column, spun down for 30 s at 8000 g and flow
351 through was discarded. Column was washed with 700 µL RW1 buffer twice, followed by two washes with
352 500 µL RPE buffer, spun down empty to remove residual buffer, transferred into a clean Eppendorf tube
353 and RNA was eluted in 30 µL of RNAse free water after incubation at 50°C for 1 minute. Next, 1 µg of RNA
354 was treated with DNAse I (Amplification grade) (ThermoFisher), and cDNA was synthesized using iScript™
355 cDNA Synthesis Kit (Bio-Rad) according to manufacturer's instructions. qRT-PCR was carried out using
356 Power SYBR™ Green PCR Master Mix (Applied Biosystems) and samples were run on 96-well plates on a
357 Bio-Rad CFX96 machine at 95°C for 3 minutes, and 40 cycles at 95°C for 5 seconds and 60°C for 15 seconds,
358 followed by a dissociation step. Primer sequences were as follows: *Nr1h2*-F: 5'-
359 CGTCCACCATTGAGATCATGT-3'; *Nr1h2*-R: 5'-GCGAGAACTCGAAGATGGGA-3'; *Nr1h3*-F: 5'-
360 GCGCTTTGCCCACTTTACTG-3'; *Nr1h3*-R: 5'-CTCCAGAAGCATGACCTCGAT-3'; *Abca1*-F: 5'-
361 GGAAGTTGGCAAGGTTGGTG-3'; *Abca1*-R: 5'-CGCCACTGTAGTTACTGGCA-3'; *β-actin*-F: 5'-
362 CGCAGCCACTGTCGAGTC-3'; *β-actin*-R: 5'-GTCATCCATGGCGAACTGGT-3'. Relative quantification was
363 carried out using ΔΔCt method, normalizing to the most efficient reaction, and relative to *β-actin*
364 expression.

365 **Body composition analysis**

366 Middle-aged adult (8-10 months) male mice were placed in EchoMRI-500 body composition analysis
367 device (EchoMRI) (Dai Pra et al., 2022). Three replicate measurements of fat mass and lean mass for each
368 animal were taken.

369 **Plasma cholesterol concentration measurements**

370 Blood samples from young adult males were collected by retroorbital venous plexus puncture or cardiac
371 puncture if terminal, after 6 hours of fasting. Plasma was separated by centrifugation and stored at -80°C
372 until analysis. Total plasma cholesterol levels were determined by standard enzymatic methods (Wako
373 Chemicals).

374 **Mouse sperm preparation and *in vitro* capacitation**

375 Epididymal spermatozoa from adult male mice (young adult (YA): 2-4 months; mature adult (MA): 5-7
376 months; middle-aged adult (MDA): 8-10 months) (Flurkey et al., 2007) were collected by swim-out from
377 cauda epididymis in HS medium (in mM: 135 NaCl, 5 KCl, 1 $MgSO_4$, 2 $CaCl_2$, 20 HEPES (pH 7.5), 5 glucose,
378 10 sodium lactate, 1 sodium pyruvate, pH 7.4 adjusted with NaOH, 320 mOsm/L), or EmbryoMax® M2
379 medium (EMD Millipore). To induce capacitation, 2×10^6 sperm/mL were incubated in human tubular fluid
380 (HTF) medium (EMD Millipore) at 37°C, 5% CO_2 for 90 min. Sperm either under uncapacitating conditions
381 (M2 or in HS) or under capacitating conditions (HTF) were treated with methyl-β-cyclodextrin (MBCD, 1.3
382 mg/mL) and polyvinyl alcohol (PVA, 1 mg/mL) for 1 hour at 37°C to examine the efficiency of cholesterol
383 efflux and its effect on capacitation (acrosome reaction) rate. In experiments where protein levels from
384 lysates from cauda, corpus and caput sperm were compared, caput sperm were purified using Percoll
385 gradients as previously described (Krapf et al., 2012; Galan et al., 2021). Briefly, sperm suspension is

386 layered over a Percoll gradient containing 45% Percoll/PBS in upper phase, and 90% Percoll/PBS in lower
387 phase, and centrifuged at 650 g for 25 minutes. Interphase contained purified caput sperm, which were
388 washed in 1x PBS and prepared for protein extraction as described below.

389 **Sperm motility analysis**

390 Aliquots of sperm were placed in slide chamber (CellVision, 20 µm depth) and motility was examined on
391 a 37°C stage of a Nikon E200 microscope under 10X phase contrast objective (CFI Plan Achro 10X/0.25 Ph1
392 BM, Nikon). Images were analyzed for spermatozoa by head tracing via computer-assisted sperm analysis
393 (CASA, Sperm Class Analyzer version 6.3, Microptic, Barcelona, Spain). Images were recorded (40 frames
394 at 50 fps) using CMOS video camera (Basler acA1300-200um, Basler AG, Ahrensburg, Germany) and
395 analyzed by computer-assisted sperm analysis (CASA, Sperm Class Analyzer version 6.3, Microptic,
396 Barcelona, Spain). Sperm motility (%) was quantified, and motion parameters including curvilinear velocity
397 (VCL, in mm/s) and amplitude of lateral head displacement (ALH, in mM) were measured. Over 200 motile
398 sperm were analyzed for each trial, with 3-4 biological replicates performed for each genotype, as denoted
399 in figure legends.

400 **Flagellar waveform analysis**

401 To tether sperm head for planar beating, non-capacitated or capacitated spermatozoa (2-3×10^5 cells) from
402 adult male mice were transferred to the fibronectin-coated 37°C chamber for Delta T culture dish
403 controller (Bioptechs) filled with HS and HEPES-buffered HTF medium (H-HTF) (Chung et al., 2017).
404 Flagellar movements of the tethered sperm were recorded for 2 s with 200 fps using pco.edge sCMOS
405 camera equipped in Axio observer Z1 microscope (Carl Zeiss). All movies were taken at 37°C within 10
406 minutes after transferring sperm to the imaging dish. FIJI software (Schindelin et al., 2012) was used to
407 generate overlaid images to trace waveform of sperm flagella as previously described (Wang et al., 2022).

408 **Sperm immunocytochemistry**

409 Sperm were washed in PBS twice, attached on glass coverslips, and fixed with 4% paraformaldehyde (PFA)
410 in PBS at room temperature (RT) for 10-15 minutes. Fixed samples were permeabilized using 0.1% Triton
411 X-100 in PBS at RT for 10 minutes and blocked with 10% normal goat serum in PBS at RT for 1 hr. Cells were
412 stained with DHCR24 (1:500, Cell Signaling Technology) or IZUMO (1:250, Bio-Academia) antibody in 10%
413 goat serum in PBS at 4°C overnight. After washing in PBS, the samples were incubated with secondary
414 antibody (1:1,000) in 10% goat serum in PBS at RT for 1 hr. Hoechst was used to counterstain nucleus.
415 Immunostained samples were mounted with Prolong gold (Invitrogen) and cured for 24 h, or with
416 VectaShield (Vector laboratories), followed by confocal imaging with Zeiss LSM710 using Plan-
417 Apochrombat 63X/1.40 or alpha Plan-APO 100X/1.46 oil objective lens (Carl Zeiss).

418 **Protein extraction and western blotting**

419 *Preparation of testis lysate*

420 Mouse testis lysate was prepared for western blotting as previously described (Hwang et al., 2019; Ded et
421 al., 2020). In short, mouse testes were homogenized in 0.32M sucrose and centrifuged at 1000 g for 10
422 min at 4°C to remove cell debris and nuclei. 1% Triton X-100 in PBS containing protease inhibitor cocktail
423 (cOmplete Mini, EDTA-free, Roche) was added to the cleared homogenates to make total testis lysate. The
424 lysates were centrifuged at 4°C, 14,000 g for 30 min and the supernatant was used for the downstream
425 experiments. For experiments measuring ABCA1 expression, testes were homogenized in 1x RIPA buffer

426 containing protease inhibitor cocktail (cOmplete Mini, EDTA-free, Roche), centrifuged at 4°C, 14,000 g for
427 30 min and the supernatant was used for the downstream experiments.

428 *Preparation of whole sperm lysate and solubilized protein extracts*

429 Whole sperm protein was extracted as previously described (Chung et al., 2011; 2014; 2017). In short,
430 mouse epididymal spermatozoa washed in PBS were directly lysed in 2× SDS or 2x LDS sample buffer. The
431 whole sperm lysate was centrifuged at 15,000 g, 4°C for 10 min. After adjusting DTT to 50 mM, supernatant
432 was denatured at 75°C for 10 min before loading to gel. Antibodies used for western blotting were rabbit
433 anti-mouse DHCR24 (1:1000, Cell Signaling Technologies), and anti-acetylated tubulin (1:20,000, Sigma).
434 Secondary antibodies were anti-rabbit IgG-HRP (1:10,000) and anti-mouse IgG-HRP (1:10,000) from
435 Jackson ImmunoResearch (West Grove, PA).

436 **Sperm lipidomics**

437 *Preparation of sperm samples*

438 Sterol biosynthesis in sperm was analyzed by liquid chromatography with tandem mass spectrometry (LC-
439 MS/MS) as described previously (Mitsche et al., 2015; Zhang et al., 2021). Sperm cells from mature adult
440 (5-7 months old) WT or *Dhcr24-TG* mice were isolated from cauda epididymis. Cells were washed with PBS
441 twice, then snap frozen in liquid N2 and stored at -80 °C.

442 *LC-MS/MS analysis*

443 Lipids were extracted from the samples by a modified Bligh–Dyer extraction, and sterols were analyzed by
444 LC-MS/MS as described previously (Zhang et al., 2021). Briefly, lipid extracts from samples were dried
445 under nitrogen and reconstituted in 90% methanol. Sterols were analyzed using a Shimadzu LC20ADxr
446 high-performance liquid chromatograph equipped with an Agilent Poroshell 120 EC-C18 column (2.1 × 150
447 mm, 2.7-µm particles; Agilent Technologies). The elution was done using a solvent gradient that
448 transitioned linearly from 93% methanol/7% H2O to 100% methanol in 7 min. The column was washed for
449 5 min in 100% methanol and then returned to the initial solvent. Sterols were detected using a SCIEX API
450 5000 triple quadrupole mass spectrometer equipped with a Turbo V APCI source in positive mode with
451 atmospheric pressure chemical ionization at a temperature of 350 °C. Data were acquired under multiple
452 reaction monitoring for mass pairs optimized for each sterol. The internal standards were commercially
453 available for all but four of the sterols (dihydro-ff-MAS, dihydro-t-MAS, dehydrolathosterol, and
454 dehydrodesmosterol) in the cholesterol biosynthetic pathway that were identified by their unique m/z
455 values and retention times as described (Mitsche et al., 2015; McDonald et al., 2012).

456 **Scanning electron microscopy**

457 Sperm cells were attached on the glass coverslips and fixed with 2.5% glutaraldehyde (GA) in 0.1 M sodium
458 cacodylate buffer (pH 7.4) for one hour at 4°C and post fixed in 2% osmium tetroxide in 0.1 M cacodylate
459 buffer (pH 7.4). The fixed samples were washed with 0.1 M cacodylate buffer for 3 times and dehydrated
460 through a series of ethanol to 100%. The samples were dried using a 300 critical point dryer with liquid
461 carbon dioxide as transitional fluid. The coverslips with dried samples were glued to aluminum stubs and
462 sputter coated with 5 nm platinum using a Cressington 208HR (Ted Pella) rotary sputter coater. Prepared
463 samples were imaged with Hitachi SU-70 scanning electron microscope (Hitachi High-Technologies).

464 **Transmitted electron microscopy**

465 Collected epididymal sperm cells were washed and pelleted by centrifugation and fixed in 2.5%
466 glutaraldehyde and 2% PFA in 0.1 M cacodylate buffer pH 7.4 for one hour at RT. Fixed sperm pellets were
467 rinsed with 0.1 M cacodylate buffer and spun down in 2% agar. The chilled blocks were trimmed, rinsed in
468 the 0.1 M cacodylate buffer, and replaced with 0.1% tannic acid in the buffer for one hour. After rinsing in
469 the buffer, the samples were post-fixed in 1% osmium tetroxide and 1.5% potassium ferrocyanide in 0.1 M
470 cacodylate buffer for one hour. The post-fixed samples were rinsed in the cacodylate buffer and distilled
471 water, followed by en bloc staining in 2% aqueous uranyl acetate for one hour. Prepared samples were
472 rinsed and dehydrated in an ethanol series to 100%. Dehydrated samples were infiltrated with epoxy resin
473 Embed 812 (Electron Microscopy Sciences), placed in silicone molds, and baked for 24 hours at 60°C. The
474 hardened blocks were sectioned in 60 nm thickness using Leica UltraCut UC7. The sections were collected
475 on grids coated with formvar/carbon and contrast stained using 2% uranyl acetate and lead citrate. The
476 grids were imaged using FEI TecnaiBiotwin Transmission Electron Microscope (FEI, Hillsbroro, OR) at 80 kV.
477 Images were taken using MORADA CCD camera and iTEM (Olympus) software.

478 **Mitochondrial membrane potential (ΔΨm) measurement**

479 1 million uncapacitated sperm from cauda epididymis in 500 µL HS were attached on Delta T chamber
480 coated with poly-D-Lysine (0.1 mg/mL). 100 nM of Mitotracker Red CMXRos (ThermoFisher), previously
481 established for MMP measurements (Pendergrass et al., 2004) including in sperm (Santiani et al., 2016),
482 was loaded into sperm for 30 min, followed by a wash with HS. Alternatively, sperm were capacitated for
483 1 hour in HTF, then HTF was replaced with H-HTF, sperm were attached on poly-D-Lysine coated Delta T
484 chamber and Mitotracker was loaded for 30 minutes, then washed with H-HTF. 10 µM of antimycin was
485 added while taking time lapse images. The images were captured by Axio observer Z1 microscope (Carl
486 Zeiss) equipped by pco.edge cMOS camera and DG-4. The data were analyzed by Zen Blue.

487 **Oxygen consumption rate measurement**

488 For extracellular flux measurement, HTF was replaced by H-HTF for capacitated sperm and M2 by HS media
489 for uncapacitated sperm. 2 million sperm per well was placed into concanavalin A (0.05 mg/mL) coated
490 96-well plate for Seahorse XFe96 (Agilent). Mitochondrial activity (OXPHOS) was measured after
491 sequential injections of 5 µM oligomycin, 1 µM FCCP, and 1 µM of rotenone and antimycin A. Three
492 measurements were taken after each injection. Basal respiration levels were calculated by subtracting
493 oxygen consumption rate (OCR) values obtained after rotenone and antimycin injection from initial OCR
494 measurements prior to injections (Balbach et al., 2020).

495 **Quantification and statistical analysis**

496 Statistical analyses were performed using Student's t-test or one-way analysis of variance (ANOVA) with
497 Tukey or Bonferroni post hoc test using Graphpad Prism 9. Differences were considered significant at *$p <$
498 0.05, **$p < 0.01$, and ***$p < 0.001$.

499 **Key resource table**

Reagent	Source	Identifier
Antibodies		
DHCR24	Cell Signaling	2033

acetylated tubulin	Sigma	T7451
IZUMO	Bio-Academia	73 045
ABCA1	Abcam	ab18180
TOM20	Santa Cruz	sc-11415
ODF2	Santa Cruz	sc-23135
Hoechst	Thermo Fisher Scientific	
goat anti-rabbit Alexa 647	Jackson ImmunoResearch	111-605-144
goat anti-rabbit Alexa 555-plus	Invitrogen	A32732
goat anti-rat Alexa 568	Invitrogen	A11077
anti-rabbit IgG-HRP	Jackson ImmunoResearch	111-035-144
anti-mouse IgG-HRP	Jackson ImmunoResearch	211-032-171
antimycin A	Sigma	A8674
methyl-β-cyclodextrin	Sigma	C4555

Acknowledgements

We thank the Yale Center for Cellular and Molecular Imaging for assistance in electron microscopy for the SEM and TEM images, Madison Gowett for sperm immunocytochemistry, Olga Blanco Prieto for technical advice with Seahorse experiments, Rafael Dai Pra and Viktor Feketa for assisting and technical advice with EchoMRI, and Elena Gracheva for sharing EchoMRI.

Additional Information

Funding

This work was supported by the start-up funds from Yale University and NIH R01HD096745 to J.-J.C., NIH R35HL155988 to Y.S. and NIH R35HL135820 and the American Heart Association (20TPA35490416) to C.F.-H.

Author contributions

Sona Relovska – Validation, Data Curation, Formal Analysis, Investigation, Visualization, Methodology, Writing – Original Draft Preparation, Writing – Review & Editing; Huafeng Wang - Validation, Data Curation, Formal Analysis, Investigation, Visualization, Methodology, Writing – Original Draft Preparation; Xinbo Zhang – Validation, Conceptualization, Data curation, Investigation; Kyung Jo Jeong – Formal Analysis, Software, Visualization; Jungmin Choi – Methodology, Visualization; Pablo Fernandez Tussy – Validation, Data Curation, Investigation, Methodology; Yajaira Suárez – Methodology, Resources, Writing – Review & Editing; Jeffrey G. McDonald – Validation, Data Curation, Formal Analysis, Methodology; Carlos Fernandez-Hernando - Conceptualization, Writing – Review & Editing, Supervision, Resources, Funding Acquisition; Jean-Ju Chung - Conceptualization, Data Curation, Formal Analysis, Investigation, Visualization, Methodology, Writing – Original Draft Preparation, Writing – Review & Editing, Project administration, Supervision, Resources, Funding Acquisition

Author ORCIDs

Sona Relovska – https://orcid.org/0000-0001-9363-1407

Huafeng Wang – https://orcid.org/0000-0002-7326-4379

Xinbo Zhang – https://orcid.org/0000-0002-9184-5767

Kyungjo Jeong – https://orcid.org/0000-0001-5210-9962
Jungmin Choi – https://orcid.org/0000-0002-8614-0973
Pablo Fernández-Tussy – https://orcid.org/0000-0002-7263-6767
Yajaira Suárez – https://orcid.org/0000-0003-4549-2953
Jeffrey G. McDonald – https://orcid.org/0000-0003-1570-4142
Carlos Fernández-Hernando – https://orcid.org/0000-0002-3950-1924
Jean-Ju Chung – https://orcid.org/0000-0001-8018-1355

Ethics

Animal experimentation: This study was performed in strict accordance with the recommendations in the Guide for the Care and Use of Laboratory Animals of the National Institutes of Health. All the mice were treated in accordance with guidelines approved by Yale (11577 to C.F.-H and 20079 to J.-J.C.) Animal Care and Use Committees (IACUC).

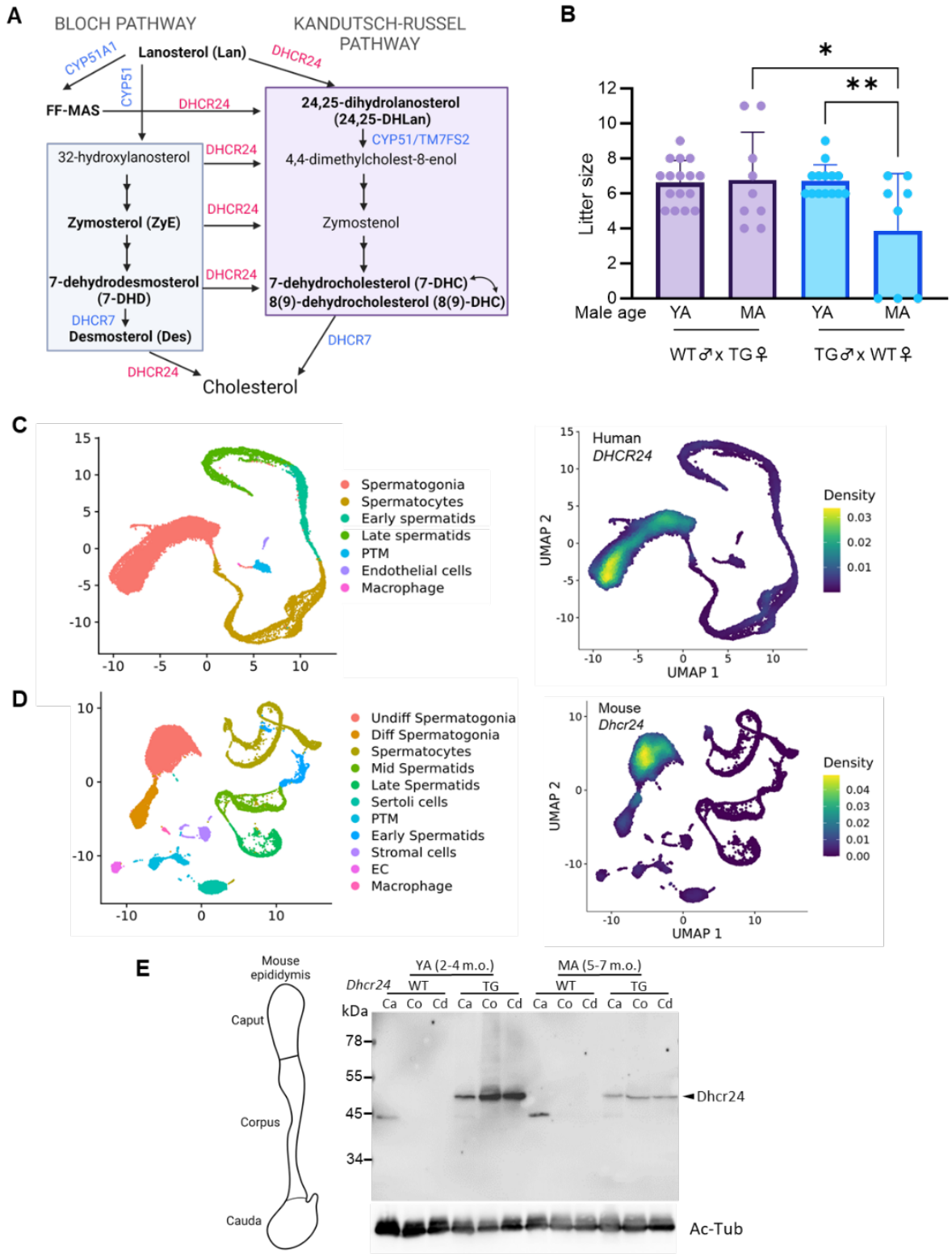

552

553 **Figure 1. DHCR24 overexpression leads to age-dependent decline in male fertility.** (**A**) Diagram showing
554 the involvement of DHCR24 in two parallel pathways to produce cholesterol: the Bloch (*left*) and
555 Kandutsch-Russel (*right*) pathways. (**B**) Litter sizes resulting from wild-type (WT) and *Dhcr24-TG* (TG)

556 crosses of young adult (YA) and mature adult (MA) mice. Error bars SD, statistical analysis one-way ANOVA.
557 (**C-D**) *Dhcr24* mRNA expression in human (C) and mouse (D) testicular cells using human (GSE109037) and
558 mouse (GSE109033) testis single-cell RNA (scRNA)-seq datasets. UMAP plots represent 7 and 11 clusters
559 of testicular cells in human and mouse (*left*) and nebula plots of *Dhcr24* mRNA expression density in these
560 clusters (*right*). EC, endothelial cell; PTM, peritubular myoid cell. (**E**) Western blot analysis of DHCR24
561 protein levels in epididymal spermatozoa from caput (Ca), corpus (Co), or cauda (Cd) of WT and *Dhcr24-*
562 *TG* young and mature adults. YA, young adult (2-4 months old); MA, mature adult (5-7 months old).
563 Illustration created with BioRender.com.

564

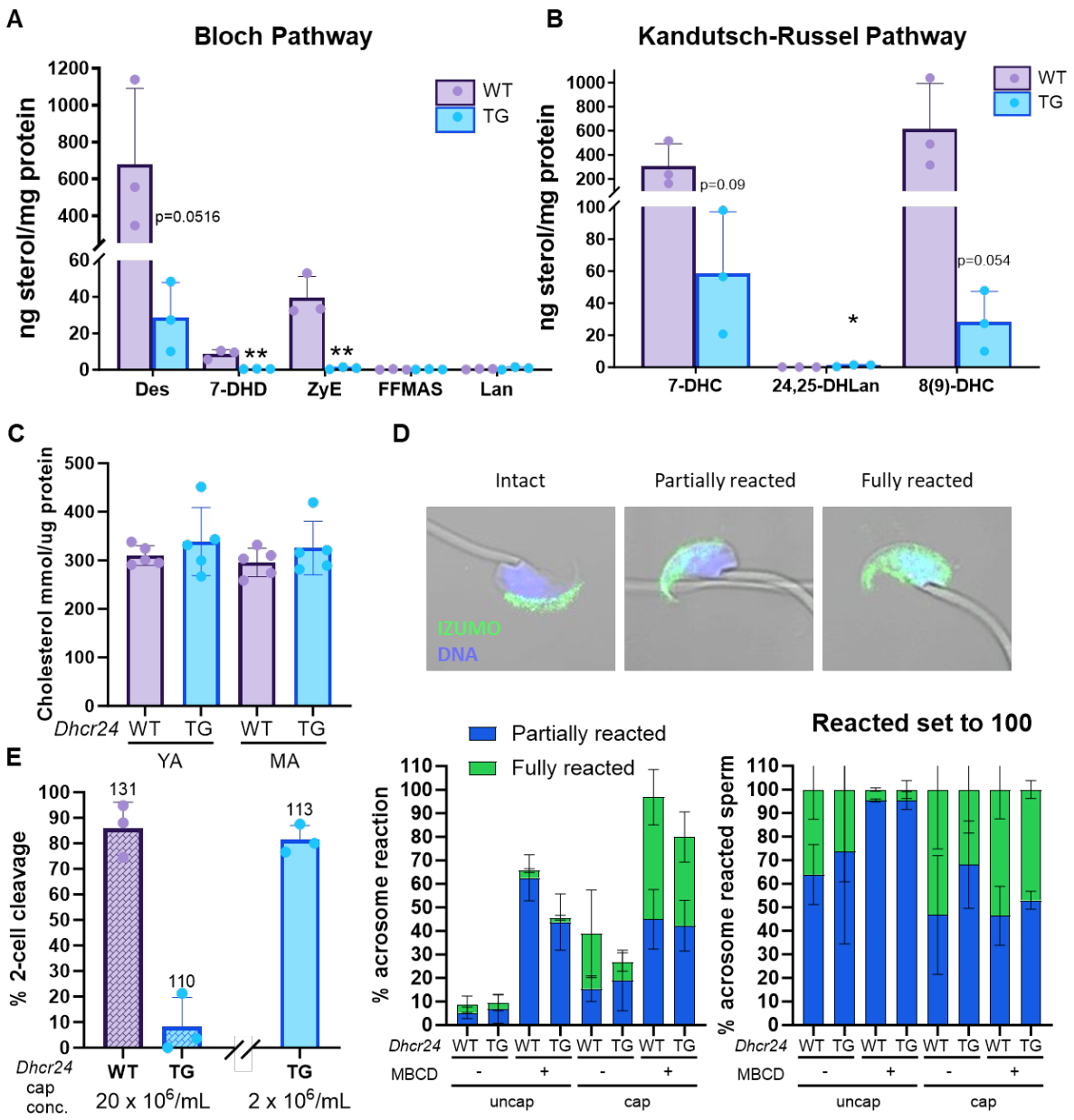

Figure 2. Dysregulated sterol biosynthesis affects sperm plasma membrane of *Dhcr24-TG* males. (**A** and **B**) Lipidomics analysis of WT and *Dhcr24-TG* (TG) sperm from mature adult mice for lipid species in Bloch (A) and Kandutsch-Russel (B) pathways. Statistical analysis student's t-test. (**C**) Cholesterol levels from the testis of WT or *Dhcr24-TG* young adult and mature adult animals. (**D**) Acrosome reaction progression by IZUMO staining. Spermatozoa from young adult WT and *Dhcr24-TG* (TG) animals were incubated under non-capacitating (uncap) or capacitating (cap) conditions in the absence (-) or presence (+) of methyl-β-cyclodextrin (MBCD). (**E**) *In vitro* fertilization using spermatozoa of WT and *Dhcr24-TG* (TG) young adult animals capacitated at high (~20x10^6 sperm/mL) or standard (2x10^6 sperm/mL) cell concentration. All error bars SD.

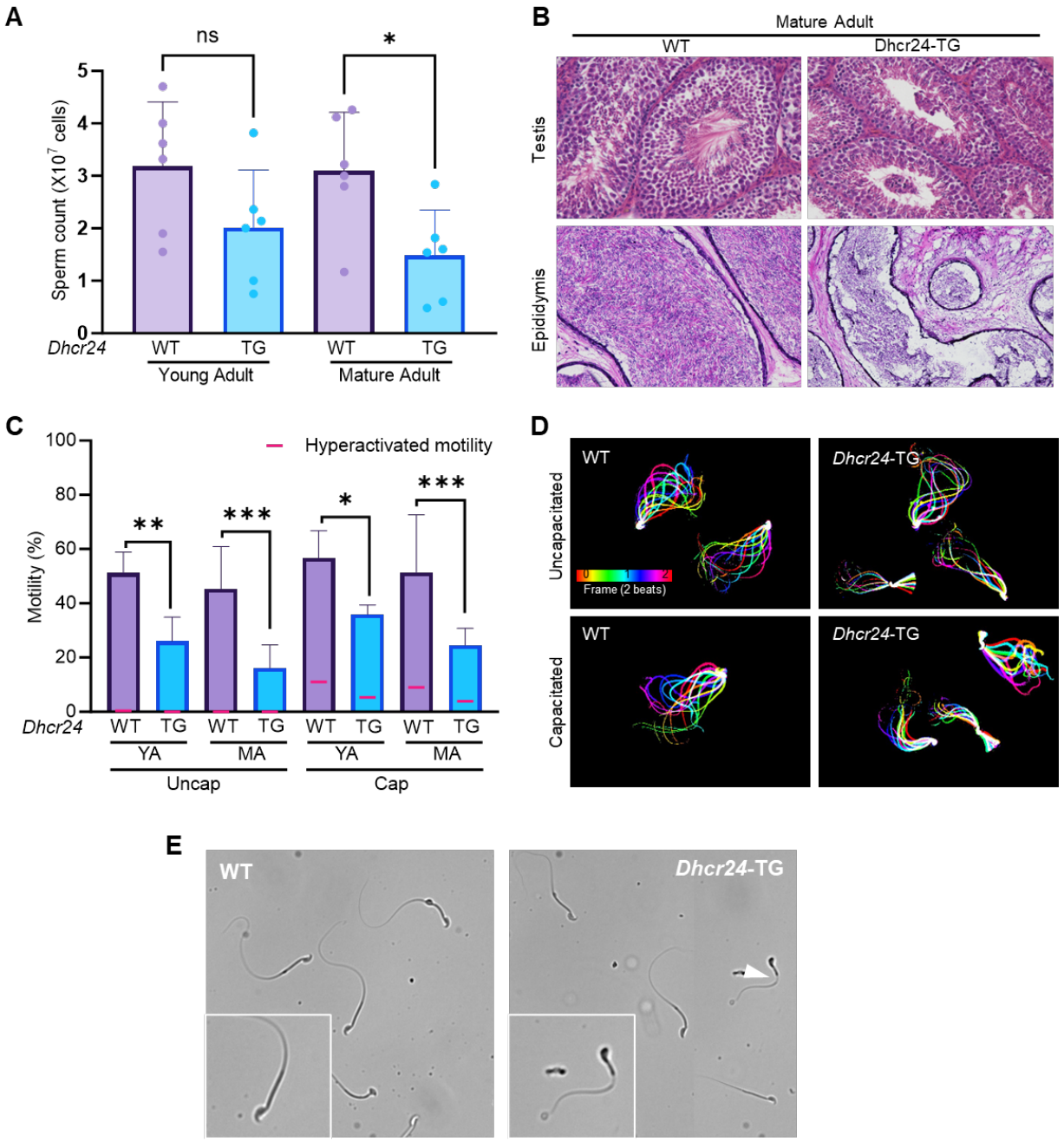

Figure 3. *Dhcr24-TG* males have decreased sperm count and motility. (**A**) Sperm counts from young and mature adult WT and *Dhcr24-TG* (TG) male mice. Statistical analysis one way ANOVA. (**B**) Hematoxylin and eosin staining of testis and epididymis from mature adult WT and *Dhcr24-TG* mice. (**C**) Total and hyperactivated motility from spermatozoa of young and mature adult WT and *Dhcr24-TG* males before and after capacitation (n=4). Statistical analysis two-way ANOVA. (**D**) Flagellar waveform analysis of WT and *Dhcr24-TG* spermatozoa before and after capacitation (mature adult). YA, young adult (2 – 4 months old); MA, mature adult (5 – 7 months old). (**E**) Brightfield images of spermatozoa from mature adult WT and *Dhcr24-TG* animals. White arrow points to thinner area between midpiece and principal piece observed in *Dhcr24-TG* sperm. All error bars SD.

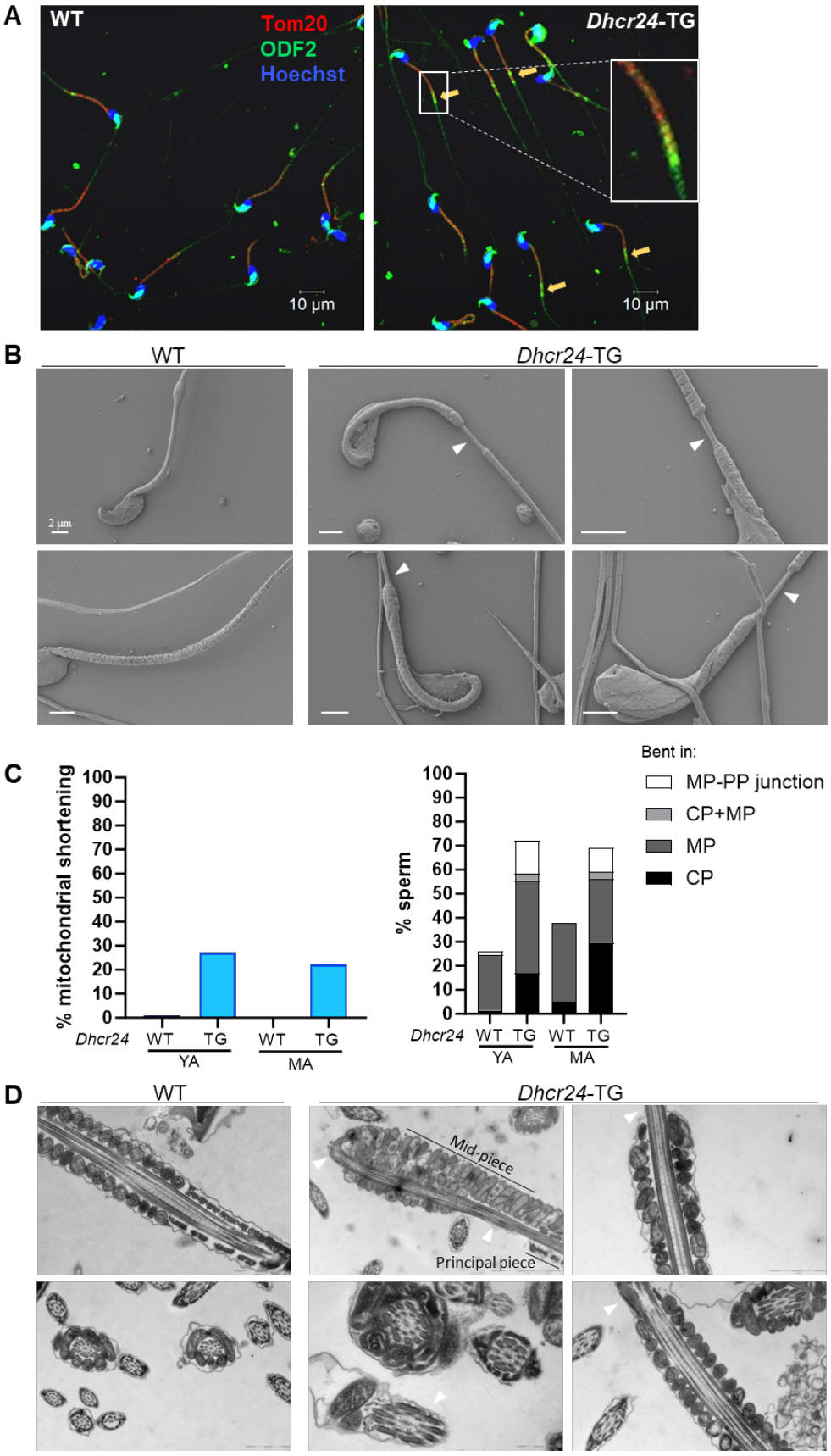
A
WT
Tom20
ODF2
Hoechst
10 µm
Dhcr24-TG
10 µm
B
WT
Dhcr24-TG
2 µm
C
% mitochondrial shortening
100
90
80
70
60
50
40
30
20
10
0
Dhcr24
WT
TG
WT
TG
YA
MA
% sperm
Bent in:
MP-PP junction
CP+MP
MP
CP
D
WT
Dhcr24-TG
Mid-piece
Principal piece

585

586 **Figure 4. Sperm from *Dhcr24-TG* mice show abnormal head bending and incomplete mitochondrial**
587 **packing.** (**A**) Immunofluorescence images of WT and *Dhcr24-TG* spermatozoa from mature adult animals
588 stained with antibodies against Tom20 (red), ODF (green) and counterstained with Hoechst detecting
589 nucleus (blue). (**B**) Scanning electron microscopy (SEM) images of WT and *Dhcr24-TG* spermatozoa from
590 mature adult animals. The bending of the head towards the midpiece can be observed in *Dhcr24-TG*
591 spermatozoa. White arrows indicate the exposed outer dense fiber (ODF) in the midpiece of *Dhcr24-TG*
592 spermatozoa. (**C**) Quantification of sperm defects in SEM images of sperm from young and mature adult
593 WT and *Dhcr24-TG* animals. *Left*, percentage of sperm with shortened mitochondrial sheath; *right*,
594 percentage of sperm with tail bending at the connecting piece (CP), midpiece (MP), both connecting piece
595 and midpiece (CP+MP), or at the junction of midpiece-principal piece (MP-PP). (**D**) Transmission Electron
596 Microscopy (TEM) images of WT and *Dhcr24-TG* spermatozoa from mature adult animals. White arrows
597 indicate the exposed outer dense fiber (ODF) in the midpiece of *Dhcr24-TG* spermatozoa. The erratic
598 mitochondrial packing along the sperm tail results in ODF exposure in the distal region of *Dhcr24-TG*
599 spermatozoa.

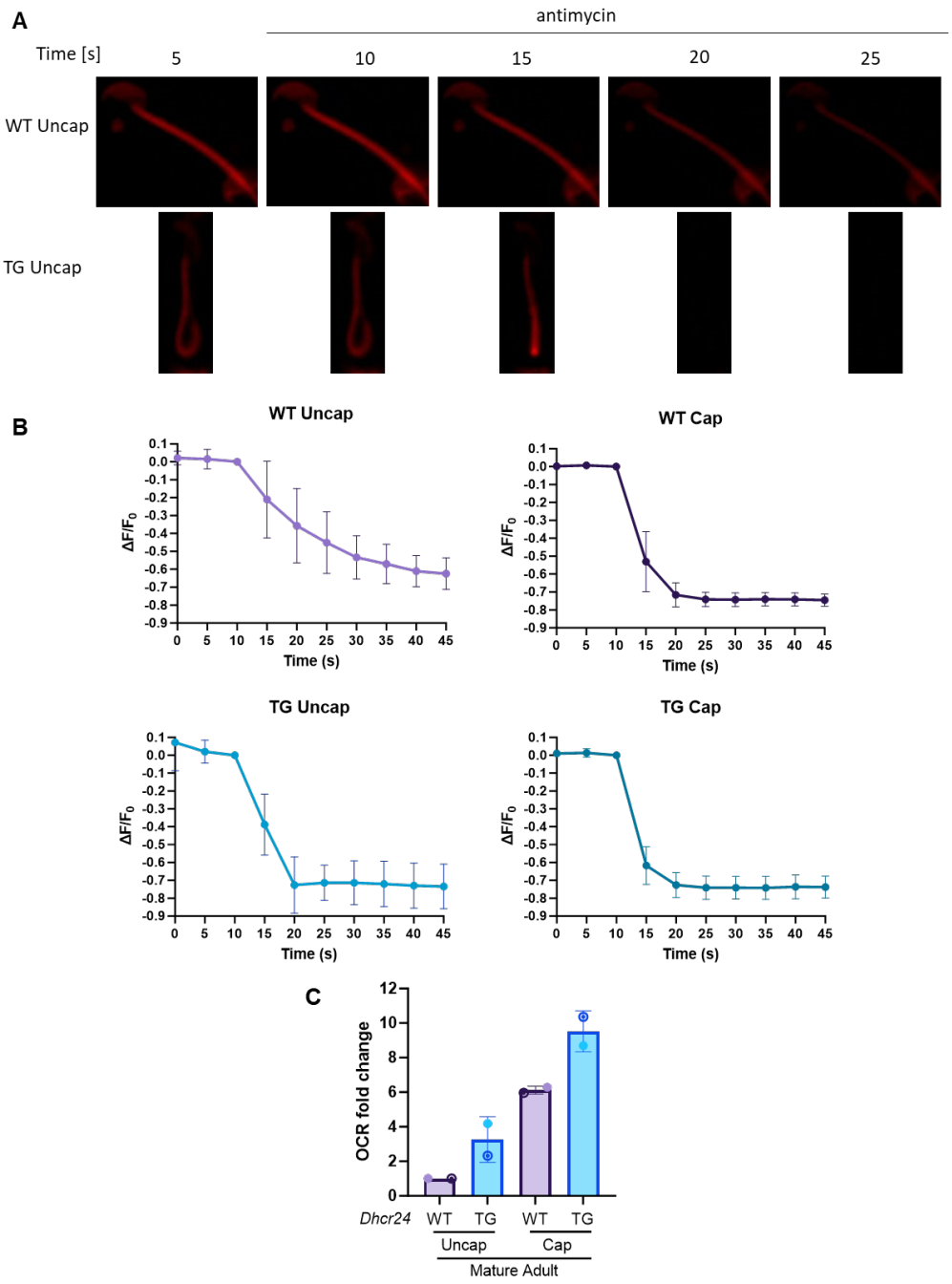

Figure 5. DHCR24 overexpression affects spermatozoan metabolism. (**A**) Dynamic representative images of mitochondrial membrane potential indicated by MitoTracker™ Red CMXRos in uncapacitated WT and *Dhcr24-TG* sperm upon antimycin treatment. (**B**) Transition of the mitochondrial membrane potential. The changes of fluorescence intensity were calculated as $\Delta F/F_0$ (F_0, the mean fluorescence intensity of the sperm midpiece before adding antimycin A (t = 10 s); F, the fluorescence of the midpiece after adding antimycin A; $\Delta F=F- F_0$). Error bars SD. (**C**) Fold change in basal respiratory oxygen consumption rate from Seahorse analysis, measurements normalized to WT uncapacitated sperm. Spermatozoa from middle aged adult. Error bars SD.

609 ## References

610 Aitken, R.J., Baker, M.A., 2006. Oxidative stress, sperm survival and fertility control. Molecular and Cellular
611 Endocrinology, POST-MEIOTIC APPROACHES TO MALE CONTRACEPTION 250, 66–69.
612 https://doi.org/10.1016/j.mce.2005.12.026

613 Andersson, H.C., Kratz, L., Kelley, R., 2002. Desmosterolosis presenting with multiple congenital anomalies
614 and profound developmental delay. American Journal of Medical Genetics 113, 315–319.
615 https://doi.org/10.1002/ajmg.b.10873

616 Balbach, M., Gervasi, M.G., Hidalgo, D.M., Visconti, P.E., Levin, L.R., Buck, J., 2020. Metabolic changes in
617 mouse sperm during capacitation†. Biology of Reproduction 103, 791–801.
618 https://doi.org/10.1093/biolre/ioaa114

619 Boerke, A., Brouwers, J.F., Olkkonen, V.M., van de Lest, C.H.A., Sostaric, E., Schoevers, E.J., Helms, J.B.,
620 Gadella, B.M., 2013. Involvement of bicarbonate-induced radical signaling in oxysterol formation and
621 sterol depletion of capacitating mammalian sperm during in vitro fertilization. Biol Reprod 88, 21.
622 https://doi.org/10.1095/biolreprod.112.101253

623 Borges, B.C., Garcia-Galiano, D., da Silveira Cruz-Machado, S., Han, X., Gavrilina, G.B., Saunders, T.L.,
624 Auchus, R.J., Hammoud, S.S., Smith, G.D., Elias, C.F., 2017. Obesity-Induced Infertility in Male Mice Is
625 Associated With Disruption of Crisp4 Expression and Sperm Fertilization Capacity. Endocrinology 158,
626 2930–2943. https://doi.org/10.1210/en.2017-00295

627 Costet, P., Luo, Y., Wang, N., Tall, A.R., 2000. Sterol-dependent Transactivation of theABC1 Promoter by the
628 Liver X Receptor/Retinoid X Receptor*. Journal of Biological Chemistry 275, 28240–28245.
629 https://doi.org/10.1074/jbc.M003337200

630 Chung, J.-J., Miki, K., Kim, D., Shim, S.-H., Shi, H.F., Hwang, J.Y., Cai, X., Iseri, Y., Zhuang, X., Clapham, D.E.,
631 2017. CatSperζ regulates the structural continuity of sperm Ca2+ signaling domains and is required for
632 normal fertility. Elife 6, e23082. https://doi.org/10.7554/eLife.23082

633 Chung, J.-J., Navarro, B., Krapivinsky, G., Krapivinsky, L., Clapham, D.E., 2011. A novel gene required for
634 male fertility and functional CATSPER channel formation in spermatozoa. Nat Commun 2, 153.
635 https://doi.org/10.1038/ncomms1153

636 Chung, J.-J., Shim, S.-H., Everley, R.A., Gygi, S.P., Zhuang, X., Clapham, D.E., 2014. Structurally distinct Ca(2+)
637 signaling domains of sperm flagella orchestrate tyrosine phosphorylation and motility. Cell 157, 808–822.
638 https://doi.org/10.1016/j.cell.2014.02.056

639 Craig, J.R., Jenkins, T.G., Carrell, D.T., Hotaling, J.M., 2017. Obesity, male infertility, and the sperm
640 epigenome. Fertility and Sterility 107, 848–859. https://doi.org/10.1016/j.fertnstert.2017.02.115

641 Dai Pra, R., Mohr, S.M., Merriman, D.K., Bagriantsev, S.N., Gracheva, E.O., 2022. Ground squirrels initiate
642 sexual maturation during hibernation. Current Biology 32, 1822-1828.e4.
643 https://doi.org/10.1016/j.cub.2022.02.032

644 Ded, L., Hwang, J.Y., Miki, K., Shi, H.F., Chung, J.-J., 2020. 3D in situ imaging of the female reproductive tract
645 reveals molecular signatures of fertilizing spermatozoa in mice. eLife 9, e62043.
646 https://doi.org/10.7554/eLife.62043

647 Dias, C., Rupps, R., Millar, B., Choi, K., Marra, M., Demos, M., Kratz, L.E., Boerkoel, C.F., 2014.
648 Desmosterolosis: an illustration of diagnostic ambiguity of cholesterol synthesis disorders. Orphanet
649 Journal of Rare Diseases 9, 94. https://doi.org/10.1186/1750-1172-9-94

650 Ferreira, J.J., Cassina, A., Irigoyen, P., Ford, M., Pietroroia, S., Peramsetty, N., Radi, R., Santi, C.M., Sapiro,
651 R., 2021. Increased mitochondrial activity upon CatSper channel activation is required for mouse sperm
652 capacitation. Redox Biol 48, 102176. https://doi.org/10.1016/j.redox.2021.102176

653 Finak, G., McDavid, A., Yajima, M., Deng, J., Gersuk, V., Shalek, A.K., Slichter, C.K., Miller, H.W., McElrath,
654 M.J., Prlic, M., Linsley, P.S., Gottardo, R., 2015. MAST: a flexible statistical framework for assessing
655 transcriptional changes and characterizing heterogeneity in single-cell RNA sequencing data. Genome
656 Biology 16, 278. https://doi.org/10.1186/s13059-015-0844-5

657 FitzPatrick, D.R., Keeling, J.W., Evans, M.J., Kan, A.E., Bell, J.E., Porteous, M.E.M., Mills, K., Winter, R.M.,
658 Clayton, P.T., 1998. Clinical phenotype of desmosterolosis. American Journal of Medical Genetics 75, 145–
659 152. https://doi.org/10.1002/(SICI)1096-8628(19980113)75:2<145::AID-AJMG5>3.0.CO;2-S

660 Flurkey, K., M. Currer, J., Harrison, D.E., 2007. Chapter 20 - Mouse Models in Aging Research, in: Fox, J.G.,
661 Davisson, M.T., Quimby, F.W., Barthold, S.W., Newcomer, C.E., Smith, A.L. (Eds.), The Mouse in Biomedical
662 Research (Second Edition), American College of Laboratory Animal Medicine. Academic Press, Burlington,
663 pp. 637–672. https://doi.org/10.1016/B978-012369454-6/50074-1

664 Galan, C., Serra, R.W., Sun, F., Rinaldi, V.D., Conine, C.C., Rando, O.J., 2021. Stability of the cytosine
665 methylome during post-testicular sperm maturation in mouse. PLoS Genet 17, e1009416.
666 https://doi.org/10.1371/journal.pgen.1009416

667 Ghanayem, B.I., Bai, R., Kissling, G.E., Travlos, G., Hoffler, U., 2010. Diet-Induced Obesity in Male Mice Is
668 Associated with Reduced Fertility and Potentiation of Acrylamide-Induced Reproductive Toxicity1. Biology
669 of Reproduction 82, 96–104. https://doi.org/10.1095/biolreprod.109.078915

670 Haidl, G., Opper, C., 1997. Changes in lipids and membrane anisotropy in human spermatozoa during
671 epididymal maturation. Human Reproduction 12, 2720–2723.
672 https://doi.org/10.1093/humrep/12.12.2720

673 Han, J., Zhao, C., Guo, H., Liu, T., Li, Y., Qi, Y., Deussing, J.M., Zhang, Y., Tan, J., Han, H., Ma, X., 2023. Obesity
674 induces male mice infertility via oxidative stress, apoptosis, and glycolysis. Reproduction 166, 27–36.
675 https://doi.org/10.1530/REP-23-0097

676 Hermann, B.P., Cheng, K., Singh, A., Roa-De La Cruz, L., Mutoji, K.N., Chen, I.-C., Gildersleeve, H., Lehle,
677 J.D., Mayo, M., Westernströer, B., Law, N.C., Oatley, M.J., Velte, E.K., Niedenberger, B.A., Fritze, D., Silber,
678 S., Geyer, C.B., Oatley, J.M., McCarrey, J.R., 2018. The Mammalian Spermatogenesis Single-Cell
679 Transcriptome, from Spermatogonial Stem Cells to Spermatids. Cell Rep 25, 1650-1667.e8.
680 https://doi.org/10.1016/j.celrep.2018.10.026

681 Hill, C., Noureldein, M., Karkhanis, P., Kinning, E., Vijay, S., Gowda, H., 2023. First case of desmosterolosis
682 diagnosed by prenatal whole exome sequencing. American Journal of Medical Genetics Part A 191, 859–
683 863. https://doi.org/10.1002/ajmg.a.63083

684 Hwang, J.Y., Mannowetz, N., Zhang, Y., Everley, R.A., Gygi, S.P., Bewersdorf, J., Lishko, P.V., Chung, J.-J., 2019.
685 Dual Sensing of Physiologic pH and Calcium by EFCAB9 Regulates Sperm Motility. Cell 177, 1480-1494.e19.
686 https://doi.org/10.1016/j.cell.2019.03.047

687 Hwang, J.Y., Nawaz, S., Choi, J., Wang, H., Hussain, S., Nawaz, M., Lopez-Giraldez, F., Jeong, K., Dong, W.,
688 Oh, J.-N., Bilguvar, K., Mane, S., Lee, C.-K., Bystroff, C., Lifton, R.P., Ahmad, W., Chung, J.-J., 2021. Genetic
689 Defects in DNAH2 Underlie Male Infertility With Multiple Morphological Abnormalities of the Sperm
690 Flagella in Humans and Mice. Frontiers in Cell and Developmental Biology 9.

691 Katib, A., 2015. Mechanisms linking obesity to male infertility. Cent European J Urol 68, 79–85.
692 https://doi.org/10.5173/ceju.2015.01.435

693 Koppers, A.J., De Iuliis, G.N., Finnie, J.M., McLaughlin, E.A., Aitken, R.J., 2008. Significance of Mitochondrial
694 Reactive Oxygen Species in the Generation of Oxidative Stress in Spermatozoa. The Journal of Clinical
695 Endocrinology & Metabolism 93, 3199–3207. https://doi.org/10.1210/jc.2007-2616

696 Korsunsky, I., Millard, N., Fan, J., Slowikowski, K., Zhang, F., Wei, K., Baglaenko, Y., Brenner, M., Loh, P.-R.,
697 Raychaudhuri, S., 2019. Fast, sensitive and accurate integration of single-cell data with Harmony. Nat
698 Methods 16, 1289–1296. https://doi.org/10.1038/s41592-019-0619-0

699 Krapf, D., Ruan, Y.C., Wertheimer, E.V., Battistone, M.A., Pawlak, J.B., Sanjay, A., Pilder, S.H., Cuasnicu, P.,
700 Breton, S., Visconti, P.E., 2012. cSrc is necessary for epididymal development and is incorporated into
701 sperm during epididymal transit. Dev Biol 369, 43–53. https://doi.org/10.1016/j.ydbio.2012.06.017

702 Leahy, T., Gadella, B.M., 2015. New insights into the regulation of cholesterol efflux from the sperm
703 membrane. Asian J Androl 17, 561–567. https://doi.org/10.4103/1008-682X.153309

704 Leisegang, K., Sengupta, P., Agarwal, A., Henkel, R., 2021. Obesity and male infertility: Mechanisms and
705 management. Andrologia 53, e13617. https://doi.org/10.1111/and.13617

706 McDonald, J.G., Smith, D.D., Stiles, A.R., Russell, D.W., 2012. A comprehensive method for extraction and
707 quantitative analysis of sterols and secosteroids from human plasma. J Lipid Res 53, 1399–1409.
708 https://doi.org/10.1194/jlr.D022285

709 Mitsche, M.A., McDonald, J.G., Hobbs, H.H., Cohen, J.C., 2015. Flux analysis of cholesterol biosynthesis in
710 vivo reveals multiple tissue and cell-type specific pathways. Elife 4, e07999.
711 https://doi.org/10.7554/eLife.07999

712 Morales, C.R., Marat, A.L., Ni, X., Yu, Y., Oko, R., Smith, B.T., Argraves, W.S., 2008. ATP-binding cassette
713 transporters ABCA1, ABCA7, and ABCG1 in mouse spermatozoa. Biochemical and Biophysical Research
714 Communications 376, 472–477. https://doi.org/10.1016/j.bbrc.2008.09.009

715 Muse, E.D., Yu, S., Edillor, C.R., Tao, J., Spann, N.J., Troutman, T.D., Seidman, J.S., Henke, A., Roland, J.T.,
716 Ozeki, K.A., Thompson, B.M., McDonald, J.G., Bahadorani, J., Tsimikas, S., Grossman, T.R., Tremblay, M.S.,
717 Glass, C.K., 2018. Cell-specific discrimination of desmosterol and desmosterol mimetics confers selective

718 regulation of LXR and SREBP in macrophages. Proceedings of the National Academy of Sciences 115,
719 E4680–E4689. https://doi.org/10.1073/pnas.1714518115

720 Nikolopoulou, M., Soucek, D.A., Vary, J.C., 1985. Changes in the lipid content of boar sperm plasma
721 membranes during epididymal maturation. Biochimica et Biophysica Acta (BBA) - Biomembranes 815,
722 486–498. https://doi.org/10.1016/0005-2736(85)90377-3

723 O'Flaherty, C., de Lamirande, E., Gagnon, C., 2006. Positive role of reactive oxygen species in mammalian
724 sperm capacitation: triggering and modulation of phosphorylation events. Free Radical Biology and
725 Medicine 41, 528–540. https://doi.org/10.1016/j.freeradbiomed.2006.04.027

726 Pendergrass, W., Wolf, N., Poot, M., 2004. Efficacy of MitoTracker Green and CMXrosamine to measure
727 changes in mitochondrial membrane potentials in living cells and tissues. Cytometry A 61, 162–169.
728 https://doi.org/10.1002/cyto.a.20033

729 Ren, D., Navarro, B., Perez, G., Jackson, A.C., Hsu, S., Shi, Q., Tilly, J.L., Clapham, D.E., 2001. A sperm ion
730 channel required for sperm motility and male fertility. Nature 413, 603–609.
731 https://doi.org/10.1038/35098027

732 Robertson, K.M., Schuster, G.U., Steffensen, K.R., Hovatta, O., Meaney, S., Hultenby, K., Johansson, L.C.,
733 Svechnikov, K., Söder, O., Gustafsson, J.-Å., 2005. The Liver X Receptor-β Is Essential for Maintaining
734 Cholesterol Homeostasis in the Testis. Endocrinology 146, 2519–2530. https://doi.org/10.1210/en.2004-
735 1413

736 Rohanizadegan, M., Sacharow, S., 2018. Desmosterolosis presenting with multiple congenital anomalies.
737 European Journal of Medical Genetics 61, 152–156. https://doi.org/10.1016/j.ejmg.2017.11.009

738 Santiani, A., Ugarelli, A., Evangelista-Vargas, S., 2016. Characterization of functional variables in epididymal
739 alpaca (Vicugna pacos) sperm using imaging flow cytometry. Anim Reprod Sci 173, 49–55.
740 https://doi.org/10.1016/j.anireprosci.2016.08.010

741 Schaaf, C.P., Koster, J., Katsonis, P., Kratz, L., Shchelochkov, O.A., Scaglia, F., Kelley, R.I., Lichtarge, O.,
742 Waterham, H.R., Shinawi, M., 2011. Desmosterolosis—phenotypic and molecular characterization of a
743 third case and review of the literature. American Journal of Medical Genetics Part A 155, 1597–1604.
744 https://doi.org/10.1002/ajmg.a.34040

745 Schindelin, J., Arganda-Carreras, I., Frise, E., Kaynig, V., Longair, M., Pietzsch, T., Preibisch, S., Rueden, C.,
746 Saalfeld, S., Schmid, B., Tinevez, J.-Y., White, D.J., Hartenstein, V., Eliceiri, K., Tomancak, P., Cardona, A.,
747 2012. Fiji: an open-source platform for biological-image analysis. Nat Methods 9, 676–682.
748 https://doi.org/10.1038/nmeth.2019

749 Selva, D.M., Hirsch-Reinshagen, V., Burgess, B., Zhou, S., Chan, J., McIsaac, S., Hayden, M.R., Hammond,
750 G.L., Vogl, A.W., Wellington, C.L., 2004. The ATP-binding cassette transporter 1 mediates lipid efflux from
751 Sertoli cells and influences male fertility. Journal of Lipid Research 45, 1040–1050.
752 https://doi.org/10.1194/jlr.M400007-JLR200

753 Spann, N.J., Garmire, L.X., McDonald, J.G., Myers, D.S., Milne, S.B., Shibata, N., Reichart, D., Fox, J.N.,
754 Shaked, I., Heudobler, D., Raetz, C.R.H., Wang, E.W., Kelly, S.L., Sullards, M.C., Murphy, R.C., Merrill, A.H.,
755 Brown, H.A., Dennis, E.A., Li, A.C., Ley, K., Tsimikas, S., Fahy, E., Subramaniam, S., Quehenberger, O., Russell,

D.W., Glass, C.K., 2012. Regulated Accumulation of Desmosterol Integrates Macrophage Lipid Metabolism and Inflammatory Responses. Cell 151, 138–152. https://doi.org/10.1016/j.cell.2012.06.054

Stuart, T., Butler, A., Hoffman, P., Hafemeister, C., Papalexi, E., Mauck, W.M., Hao, Y., Stoeckius, M., Smibert, P., Satija, R., 2019. Comprehensive Integration of Single-Cell Data. Cell 177, 1888-1902.e21. https://doi.org/10.1016/j.cell.2019.05.031

van Dijk, D., Sharma, R., Nainys, J., Yim, K., Kathail, P., Carr, A.J., Burdziak, C., Moon, K.R., Chaffer, C.L., Pattabiraman, D., Bierie, B., Mazutis, L., Wolf, G., Krishnaswamy, S., P'er, D., 2018. Recovering Gene Interactions from Single-Cell Data Using Data Diffusion. Cell 174, 716-729.e27. https://doi.org/10.1016/j.cell.2018.05.061

Visconti, P.E., Galantino-Homer, H., Ning, X., Moore, G.D., Valenzuela, J.P., Jorgez, C.J., Alvarez, J.G., Kopf, G.S., 1999. Cholesterol Efflux-mediated Signal Transduction in Mammalian Sperm: β-CYCLODEXTRINS INITIATE TRANSMEMBRANE SIGNALING LEADING TO AN INCREASE IN PROTEIN TYROSINE PHOSPHORYLATION AND CAPACITATION*. Journal of Biological Chemistry 274, 3235–3242. https://doi.org/10.1074/jbc.274.5.3235

Visconti, P.E., 2012. Sperm Bioenergetics in a Nutshell. Biology of Reproduction 87, 72, 1–4. https://doi.org/10.1095/biolreprod.112.104109

Venkateswaran, A., Laffitte, B.A., Joseph, S.B., Mak, P.A., Wilpitz, D.C., Edwards, P.A., Tontonoz, P., 2000. Control of cellular cholesterol efflux by the nuclear oxysterol receptor LXRα. Proceedings of the National Academy of Sciences 97, 12097–12102. https://doi.org/10.1073/pnas.200367697

Volle, D.H., Mouzat, K., Duggavathi, R., Siddeek, B., Déchelotte, P., Sion, B., Veyssière, G., Benahmed, M., Lobaccaro, J.-M.A., 2007. Multiple Roles of the Nuclear Receptors for Oxysterols Liver X Receptor to Maintain Male Fertility. Molecular Endocrinology 21, 1014–1027. https://doi.org/10.1210/me.2006-0277

Wang, H., Dou, Q., Jeong, K.J., Choi, J., Gladyshev, V.N., Chung, J.-J., 2022. Redox regulation by TXNRD3 during epididymal maturation underlies capacitation-associated mitochondrial activity and sperm motility in mice. Journal of Biological Chemistry 298, 102077. https://doi.org/10.1016/j.jbc.2022.102077

Wechsler, A., Brafman, A., Shafir, M., Heverin, M., Gottlieb, H., Damari, G., Gozlan-Kelner, S., Spivak, I., Moshkin, O., Fridman, E., Becker, Y., Skaliter, R., Einat, P., Faerman, A., Björkhem, I., Feinstein, E., 2003. Generation of Viable Cholesterol-Free Mice. Science 302, 2087–2087. https://doi.org/10.1126/science.1090776

Zalata, A., Hassan, A., Christophe, A., Comhaire, F., Mostafa, T., 2010. Cholesterol and desmosterol in two sperm populations separated on Sil-Select gradient. International Journal of Andrology 33, 528–535. https://doi.org/10.1111/j.1365-2605.2009.00961.x

[a]Zhang, X., McDonald, J.G., Aryal, B., Canfrán-Duque, A., Goldberg, E.L., Araldi, E., Ding, W., Fan, Y., Thompson, B.M., Singh, A.K., Li, Q., Tellides, G., Ordovás-Montanes, J., García Milian, R., Dixit, V.D., Ikonen, E., Suárez, Y., Fernández-Hernando, C., 2021. Desmosterol suppresses macrophage inflammasome activation and protects against vascular inflammation and atherosclerosis. Proc. Natl. Acad. Sci. U.S.A. 118, e2107682118. https://doi.org/10.1073/pnas.2107682118

[b]Zhang, H., Shen, Y., Kim, I., Weintraub, N.L., Tang, Y., 2021. The Impaired Bioenergetics of Diabetic Cardiac Microvascular Endothelial Cells. Frontiers in Endocrinology 12.

Zolotushko, J., Flusser, H., Markus, B., Shelef, I., Langer, Y., Heverin, M., Björkhem, I., Sivan, S., Birk, O.S., 2011. The desmosterolosis phenotype: spasticity, microcephaly and micrognathia with agenesis of corpus callosum and loss of white matter. Eur J Hum Genet 19, 942–946. https://doi.org/10.1038/ejhg.2011.74